Aeroacoustics Conferences
26-29 May 2026, Brussels, Belgium
32nd AIAA/CEAS Aeroacoustics Conference (2026)

10.2514/6.2026-3403

Non-linear Acoustic Signature of an Unducted Single Fan on the Fuselage

Giovanni Coco*
École Centrale de Lyon, CNRS, Université Claude Bernard Lyon 1, INSA Lyon, LMFA, UMR5509, 69130 Écully, France
Safran Aircraft Engines, Rond Point René Ravaud - Réau, 77550 Moissy-Cramayel, France

Didier Dragna† and Christophe Bailly‡
École Centrale de Lyon, CNRS, Université Claude Bernard Lyon 1, INSA Lyon, LMFA, UMR5509, 69130 Écully, France

Hélène Posson§
Safran Aircraft Engines, Rond Point René Ravaud - Réau, 77550 Moissy-Cramayel, France

Noise generated by an aero-engine propagates toward the fuselage, possibly with non-linear effects, and is then refracted by the turbulent boundary layer and scattered by the fuselage shape. As a result, the acoustic loading on the fuselage is modified compared a to free-field linear radiation. A numerical investigation into the non-linear propagation of sound waves generated by an unducted single fan engine and their interaction with the boundary layer on the fuselage surface is performed. The study aims to evaluate the influence of non-linear propagation effects and to quantify the acoustic shielding provided by the fuselage boundary layer through a parametric analysis of its thickness. The non-linear Euler equations are solved in a three-dimensional Cartesian grid using a low-dispersion and low-dissipation high order finite-difference numerical scheme, combined with an original source term formulation to model the source and the fuselage. The results show that non-linear effects associated with weak shock waves lead to a modest reduction in the Sound Pressure Level (SPL) on the fuselage, with a local decrease of up to 5 dB observed for waves propagating upstream against the flow, confined to the upstream shadow region of the fuselage and not significantly affecting the global peak levels of interest. More significantly, the fuselage boundary layer is found to provide strong acoustic shielding by refracting incoming sound waves. A parametric study was conducted considering both laminar and turbulent boundary layer profiles. For the laminar boundary layer case, as the boundary layer thickness increases, the SPL on the fuselage progressively decreases, especially in the upstream region and in the shadow zone, with a maximum reduction of nearly 40 dB observed for the thickest boundary layer tested. In contrast, the turbulent boundary layer, which is more representative of realistic cruise conditions, exhibits a less pronounced shielding effect, with SPL reductions reaching up to nearly 25 dB in the upstream and shadow regions. This reduced effectiveness highlights the impact of boundary layer state on acoustic shielding. Overall, the shielding effect also reduces the amplitude of diffraction lobes and concentrates the acoustic signature in the region directly exposed to the engine.

I. Introduction

Unducted aero-engines are currently investigated to reduce environmental footprint of aviation. Given the absence of a nacelle including acoustic liners around the fan blades and the outlet guide vane (OGV), the propagation of shock-waves generated by the blades and their impact on the fuselage need to be characterized. A tonal noise study for free-field propagation was carried out by Lewis *et al.* [1] using a hybrid approach that couples an Unsteady Reynolds-averaged Navier-Stokes (URANS) simulation with the Ffowcs-Williams Hawkings integral formulation. This methodology is representative of the current state of the art for rotating systems, where RANS simulations are commonly combined with the FWH acoustic analogy.

*PhD, Safran Aircraft Engines, giovanni.coco@ec-lyon.fr
†Assistant Professor, LMFA, École Centrale de Lyon, didier.dragna@ec-lyon.fr
‡Professor, LMFA, École Centrale de Lyon, christophe.bailly@ec-lyon.fr, AIAA Senior Member
§PhD Research Engineer, Safran Aircraft Engines, helene.de-laborderie@safrangroup.com

For configurations with unducted rotors, the interaction between the engine sound field and the airframe, commonly referred to as installation effects, can influence the acoustic loads on the fuselage surface. Installation effects may also alter the noise generation mechanisms at the source. In the present work, these source-related effects are not addressed: the acoustic source is assumed to be known a priori and is prescribed as an input to the Computational Aeroacoustics (CAA) simulations. The analysis therefore focuses exclusively on installation effects associated with sound propagation and scattering. In this context, a central element of the interaction is the fuselage and its turbulent boundary layer, which can refract and scatter the incoming acoustic waves.

Early studies established the fundamental approaches for analyzing these phenomena. Initial two-dimensional models, using plane-wave sources and step-function velocity profiles, showed that the fuselage boundary layer could provide strong acoustic shielding, especially at high cruise Mach numbers [2]. This work was soon extended through more comprehensive three-dimensional theories that represented the fuselage as an infinitely long rigid cylinder. Studies including Hanson *et al.* [3], Lu [4], and McAninch *et al.* [5] combined near-field propeller source models with numerical solutions of wave propagation inside the boundary layer, consistently predicting significant sound attenuation on the forward fuselage surface. A major difficulty in these formulations was the critical layer singularity in the governing equations, which was resolved through Frobenius series solutions. These models were later validated against flight test data [6], showing good agreement and confirming the importance of accounting for boundary layer effects in noise prediction.

Subsequent contributions refined these models by enhancing source representation, geometric details, and solution methods. Because simplified point sources can introduce large errors, studies by Belyaev [7], Brouwer [8], and Gaffney *et al.* [9] employed more realistic distributed sources, including detailed propeller models, contra-rotating open rotors, and spinning ducted fan modes, respectively. While most analytical models are restricted to circular fuselages, Schippers *et al.* [10] developed a hybrid finite element approach that accommodates non-circular cross-sections, showing that geometry can strongly affect the radiated sound field. In parallel, to reduce the cost of numerical integration, Rouvas *et al.* [11] proposed analytical models with simplified linear or step-function velocity profiles. These were shown to approximate the refraction produced by more realistic turbulent power-law profiles, particularly when the shape factor is matched.

While most previous studies examined refraction through a steady mean boundary layer, the critical role of turbulence has also been emphasized. Dierke *et al.* [12] and Siefert *et al.* [13] solved the linearized Euler equations, introducing stochastic turbulent fluctuations with the random-particle-method. Their results showed that scattering by unsteady turbulent vortices strongly modifies the surface pressure field, increasing sound levels in the shadow zone, shifting energy to higher frequencies through Doppler effects, and producing spectral broadening or haystacking.

At a more fundamental level, Howe [14] argued that wall shear stress fluctuations, often regarded as dipole sound sources, contribute to acoustic propagation rather than generation. His analysis suggests that surface shear stress reduces, rather than enhances, boundary layer noise radiation, particularly at low Mach numbers, providing theoretical support for the boundary layer's role in shaping the sound field.

Despite these advances, most studies still rely on linearized formulations, such as the Pridmore–Brown equation [15] or the linearized Euler equations, which neglect non-linear propagation effects. Moreover, investigations addressing the most recent unducted single fan configurations remain scarce in the literature [16–21]. Among these, the work of Proskurov *et al.* [22] investigates the acoustic signature on the fuselage by using a frequency domain fast multipole boundary element method, though it neglects the influence of the boundary layer.

The present study extends previous investigations by considering the non-linear propagation of sound from an unducted single fan through the resolution of the full Euler equations. This approach enables the evaluation of sound levels on the fuselage surface while capturing potential non-linear effects induced by propagation through the strong shear of the boundary layer, though the turbulent field is neglected. Particular focus is placed on the role of boundary layer thickness, a parameter identified as critical in earlier studies, to provide a more comprehensive understanding of the acoustic environment on the aircraft fuselage.

II. Numerical Setup

The three-dimensional non-linear Euler equations are solved in their conservative form written in Cartesian coordinates:

$$\frac{\partial \boldsymbol{U}}{\partial t} + \frac{\partial \boldsymbol{E}}{\partial x} + \frac{\partial \boldsymbol{F}}{\partial y} + \frac{\partial \boldsymbol{G}}{\partial z} = \boldsymbol{\Lambda}, \tag{1}$$

with

$$\begin{aligned}
\boldsymbol{U} &= (\rho, \rho u, \rho v, \rho w, \rho e_t) \\
\boldsymbol{E} &= \Big(\rho u, \rho u^2 + p, \rho u v, \rho u w, u\,(\rho e_t + p)\Big) \\
\boldsymbol{F} &= \Big(\rho v, \rho u v, \rho v^2 + p, \rho v w, v\,(\rho e_t + p)\Big) \\
\boldsymbol{G} &= \Big(\rho w, \rho u w, \rho v w, \rho w^2 + p, w\,(\rho e_t + p)\Big) \\
\boldsymbol{\Lambda} &= \left(\Lambda_\rho, \Lambda_{\rho u}, \Lambda_{\rho v}, \Lambda_{\rho w}, \Lambda_{\rho e_t}\right)
\end{aligned}$$

where $\boldsymbol{x} = (x, y, z)$ is the spatial coordinate, t is time, ρ is density, p is pressure, $\boldsymbol{u} = (u, v, w)$ is the velocity field, e_t is the total energy per mass unit, $\boldsymbol{U}$ is the unknown vector of conservative variables, $\boldsymbol{E}$, $\boldsymbol{F}$, and $\boldsymbol{G}$ are the fluxes vectors, $\boldsymbol{\Lambda}$ is the source term vector defined over a cylindrical control surface around the rotor defined by $f(\boldsymbol{x}_s) = 0$. The fuselage is represented in the simulation through a formulation of volumetric source terms designed to model reflection and diffraction effects. In this approach, the fuselage is approximated as a cylindrical surface.

Note that the equations are solved for perturbative variables with respect to a given based flow. The variables are initialized with their ambient values, that is $\boldsymbol{U}(\mathbf{x}, t = 0) = (\rho_0, \rho_0 u_0, \rho_0 v_0, \rho_0 w_0, (\rho e_t)_0)$, where the notation $(\cdot)_0$ denotes the base flow quantities, assumed to be known as the governing equations are formulated exclusively for perturbations.

The Euler equations are solved on a uniformly spaced Cartesian grid, with $\Delta x = \Delta y = \Delta z$ where Δx, Δy, Δz are the grid sizes in the x-, y-, and z- direction, respectively. Spatial derivatives are evaluated using a fourth-order, 11-point finite difference scheme with low dispersion and dissipation [23]. Time integration is carried out with a six-stage, fourth-order low-storage Runge–Kutta scheme. The source terms for the Euler equations are evaluated using the formulation given by Coco *et al.* [24], which ensures that the imposed acoustic field propagates only outward from the control surface. The source terms are introduced at the final sub-step of each iteration. A selective 11-point filter is applied across the domain to suppress spurious grid-to-grid oscillations. Perfectly Matched Layers (PML) [25] are implemented at the domain boundaries to damp outgoing acoustic waves. All simulations are performed with a Courant–Friedrichs–Lewy number of 0.5. The computational domain is discretized using a structured grid of $401 \times 349 \times 616$ points in the x-, y-, and z-directions, respectively. For each simulation, three full engine revolutions are performed to ensure that transient effects have dissipated prior to the evaluation of the Sound Pressure Level (SPL). The total computational time amounts to approximately 13 hours, achieved through OpenMP parallelization on a single compute node equipped with 64 processing cores.

In the present work, the conservative variables field introduced into the computational domain is obtained from a RANS simulation performed with the isolated rotor configuration. This simulation is carried out using the elsA Computational Fluid Dynamics solver [26]. The calculation is performed on a single blade-passage rotor-alone configuration, which is then reconstructed over 360° by applying periodicity in the azimuthal direction. The resulting signal is interpolated onto the cylindrical control surface of radius $R_s > R$, where R denotes the rotor radius. The cylindrical control surface is shown in Fig. 1. The rotor plane lies in the plane $x = 0$. The perturbation field $(\rho', (\rho u_i)', (\rho e_t)', p')$ at each point on the cylindrical surface is computed by subtracting the azimuthal mean from the conservative variables extracted from the RANS simulation.

A schematic of the computational domain is shown in Fig. 2. The left side contains the cylindrical control surface enclosing the unducted single fan, while the fuselage is positioned on the right side. The reference frame is defined as a right-handed orthogonal coordinate system. The x-axis is aligned with the cylinder axis and oriented in the direction of the incoming flow velocity. The y-axis is directed vertically upward, toward increasing altitude, while the z-axis completes the triad as the horizontal transverse direction. The simulation is conducted under cruise conditions, with a fixed uniform freestream Mach number $M_x \in [0.75, 0.8]$ aligned along the x-axis and no incidence. The fuselage is modeled as a cylinder of radius R_f, located at a distance d from the engine, and is surrounded by a uniform boundary layer of thickness δ. The angle θ is defined with respect to the center of the fuselage, and specifies the angular position on its surface. It increases counterclockwise, with $\theta = 0$ corresponding to the side of the fuselage shielded from the engine and $\theta = \pi$ corresponding to the side facing the engine.

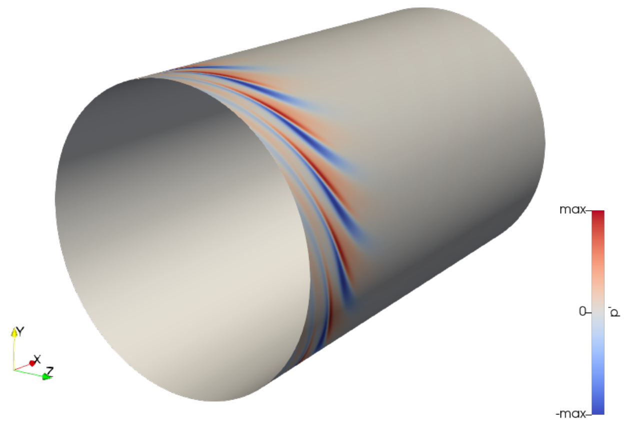

Fig. 1 Isometric view of the normalized fluctuating pressure field extracted from the RANS simulation for an unducted single fan on a cylindrical control surface.

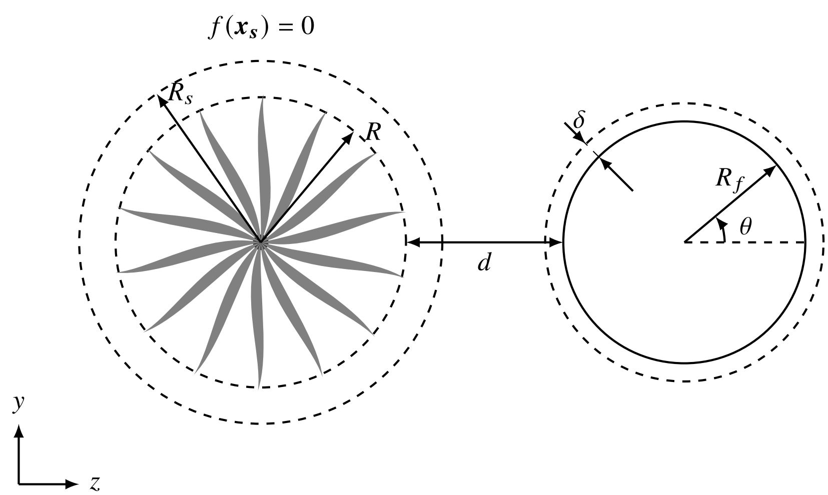

Fig. 2 Sketch of the computational domain on the yz-plane at $x = 0$. On the left, the unducted single fan with radius R and the cylindrical control surface of radius R_s where the sources are defined. On the right, fuselage with radius R_f, located at a distance d from the engine, surrounded by a uniform boundary layer of thickness δ.

III. Results

Three sets of numerical simulations were performed. The first is designed to assess the presence of non-linear effects and their influence on the fuselage acoustic signature. Specifically, the objective is to quantify the differences between linear and non-linear effects in the propagation of shock waves generated by the unducted single fan, based on the analysis of the SPL on the external surface of the fuselage. The second and third sets focus on the role of the boundary layer in shaping the acoustic signature, considering laminar and turbulent boundary layer conditions, respectively. A parametric investigation is performed to evaluate the effect of boundary layer thickness on the resulting pressure footprint.

Due to data sensitivity and confidentiality constraints, absolute values of the reported quantities are not disclosed. The presented plots retain the original data scaling but omit absolute axis values; only the variation range is indicated. Therefore, the figures should be interpreted in terms of relative variations rather than absolute magnitudes.

A. Assessment of non-linear effects

In an unducted single fan engine, weak shock waves may form at the blade tips under cruise conditions. The Euler equations account for non-linear propagation effects, which, although small, slightly alter the acoustic signature on the fuselage.

To accurately evaluate their influence, two simulations were carried out. In the first, the source terms were prescribed to reproduce the conservative variable field on the cylindrical control surface extracted from the RANS simulation. In the second, the same source terms were reduced by a factor of 100, effectively removing non-linear effects from propagation. In both cases, the fuselage was modeled without the presence of a boundary layer and assuming slip flow over its surface. The quantity $\Delta\mathrm{SPL}_{NL}$ is introduced:

$$\Delta\mathrm{SPL}_{NL} = \mathrm{SPL}_{L} - \mathrm{SPL}_{NL} \tag{2}$$

where SPL_L and SPL_{NL} are the SPL for the linear and the non-linear simulation, respectively. The SPL is computed on the fuselage surface for both simulations. The distribution of $\Delta\mathrm{SPL}_{NL}$ over the entire fuselage is presented in Fig. 3. As a reminder, the engine rotor lies in the plane $x = 0$, the engine-facing side corresponds to $\theta = \pi$, and the mean flow direction is from negative to positive x-values. Non-linear effects are more pronounced upstream of the rotor, for negative x, and within the shadow region corresponding to $\theta \in [-\pi/2, \pi/2]$.

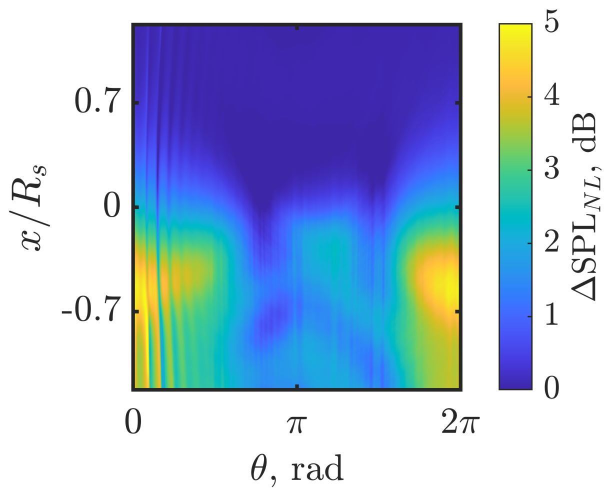

Fig. 3 Difference in $\Delta\mathrm{SPL}_{NL}$ on the fuselage surface.

For a more detailed comparison, the sound pressure levels and the corresponding $\Delta\mathrm{SPL}_{NL}$ are plotted as functions of x at $\theta = \pi$ in Figs. 4(a) and 4(b), respectively. The results indicate that non-linear effects are most pronounced upstream of the engine, where acoustic waves propagate against the mean flow. For the case considered, these effects lead to a maximum reduction of 1.8 dB in the SPL on the fuselage at $\theta = \pi$. For waves propagating with the flow, that is in the positive x-direction, non-linear effects are negligible, with variations on the order of 0.1 dB.

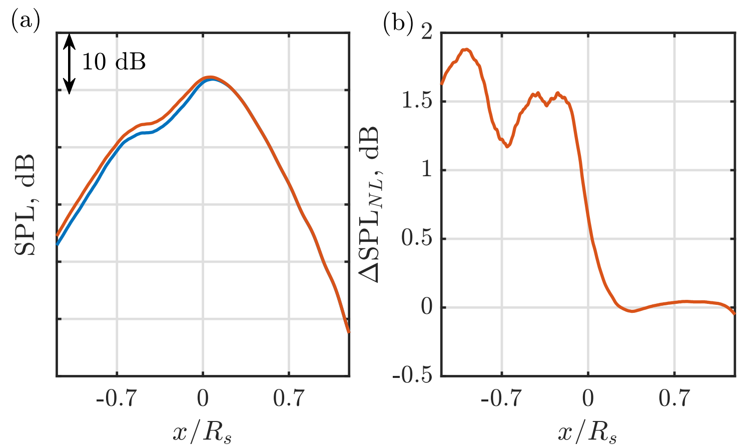

Fig. 4 (a) Sound Pressure Level and (b) difference $\Delta\mathrm{SPL}_{NL}$ between non-linear (blue) and linear (orange) behavior on the fuselage along the x-axis at $\theta = \pi$.

The SPL and $\Delta\mathrm{SPL}_{NL}$ distributions along the x-direction within the shadow region at $\theta = 0$ are shown in Figs. 5(a) and 5(b), respectively. In this region, non-linear effects are more significant, with a maximum difference of approximately 5 dB between the linear and non-linear solutions observed upstream of the engine. This peak exceeds the corresponding value at $\theta = \pi$. This behavior can be attributed to the longer propagation distance required for the shock waves to reach the shadow region. When combined with convection effects associated with the presence of a uniform flow, these conditions enhance non-linear effects on propagation.

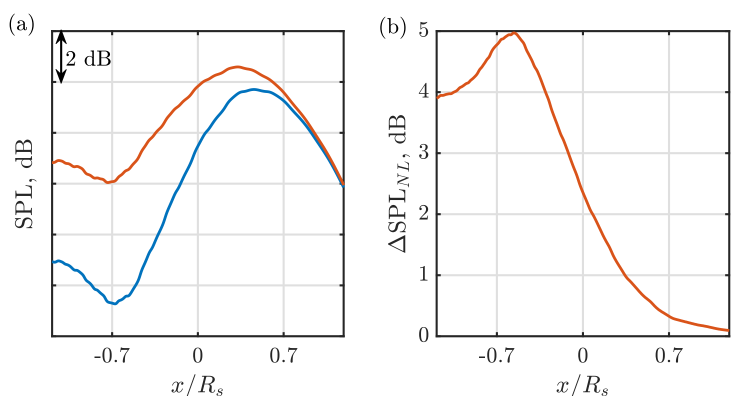

Fig. 5 (a) Sound Pressure Level and (b) difference $\Delta\mathrm{SPL}_{NL}$ between non-linear (blue) and linear (orange) behavior on the fuselage along the x-axis at $\theta = 0$.

Figures 6(a) and 6(b) present, respectively, the SPL obtained from the two simulations and the corresponding $\Delta\mathrm{SPL}_{NL}$ as functions of the angular coordinate θ on the rotor plane located at $x = 0$. As previously noted, non-linear effects intensify when approaching the shadow region on the fuselage, reaching a maximum difference of approximately 2.5 dB at $\theta = 0$. These effects become more pronounced when the same distribution is evaluated on yz-planes located further upstream of the engine, whereas they diminish on planes situated further downstream.

B. Boundary Layer Effects

The boundary layer around the fuselage strongly modifies its acoustic signature, as mentioned in Introduction. This shielding effect arises because the velocity gradient near the wall refracts upstream-propagating acoustic waves away from the fuselage [11]. The ratio of acoustic wavelength to boundary layer thickness plays a central role in this

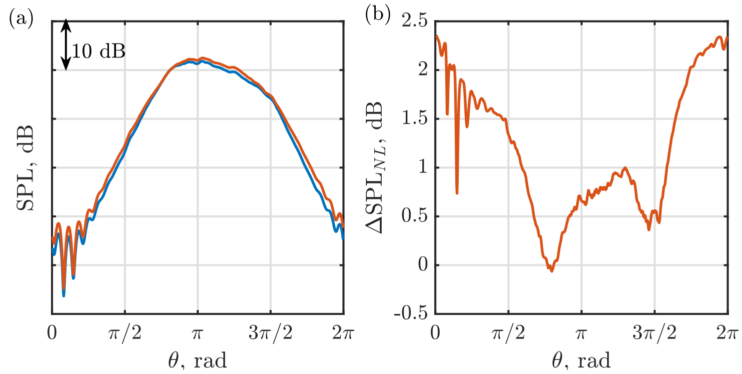

Fig. 6 (a) Sound Pressure Level and (b) difference $\Delta\mathrm{SPL}_{NL}$ between non-linear (blue) and linear (orange) behavior on the fuselage along the θ-coordinate at $x = 0$.

process: refraction becomes more pronounced when the wavelength is comparable to or smaller than the boundary layer thickness [9]. Two sets of numerical simulations were conducted to investigate boundary layer effects: one employing a laminar profile and the other employing a turbulent profile. It should be emphasized, however, that given the Reynolds numbers involved, the boundary layer is physically expected to be turbulent; the laminar case is therefore considered as an idealized reference configuration for comparison purposes.

1. Smooth parametrized boundary layer profile

A parametric study is conducted to assess the influence of the boundary layer thickness δ on the fuselage SPL. The length δ is defined as the wall-normal distance at which the velocity reaches 95% of the free-stream velocity. The laminar boundary layer velocity profile around the fuselage is chosen as follows:

$$u(r) = u_0 \tanh\left[2\left(r - R_f\right)/\delta\right], \quad r \geq R_f \tag{3}$$

where u_0 is the mean flow, R_f is the fuselage radius, and $r = \sqrt{(z - z_f)^2 + (y - y_f)^2}$ is the distance from the center of the fuselage (z_f, y_f) in the yz-plane. This profile allows to properly parametrize the mean velocity gradient for numerical simulations, as shown in Fig. 7. This formulation does not aim to reproduce an exact laminar boundary layer solution, but rather provides a smooth and parametrizable velocity distribution with a comparable gradient, suitable for assessing the sensitivity of the acoustic response.

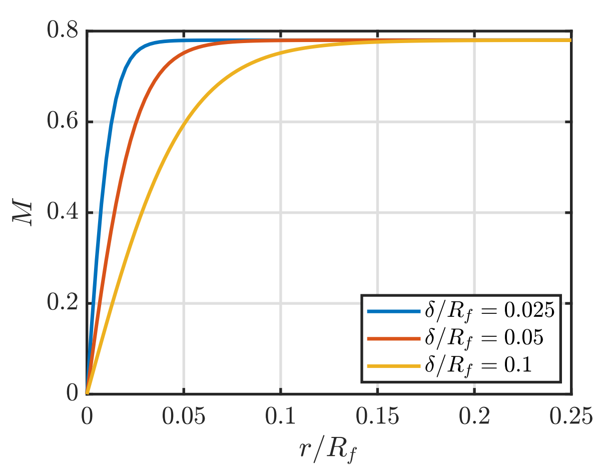

Fig. 7 Laminar boundary-layer velocity profiles for different thicknesses δ/R_f.

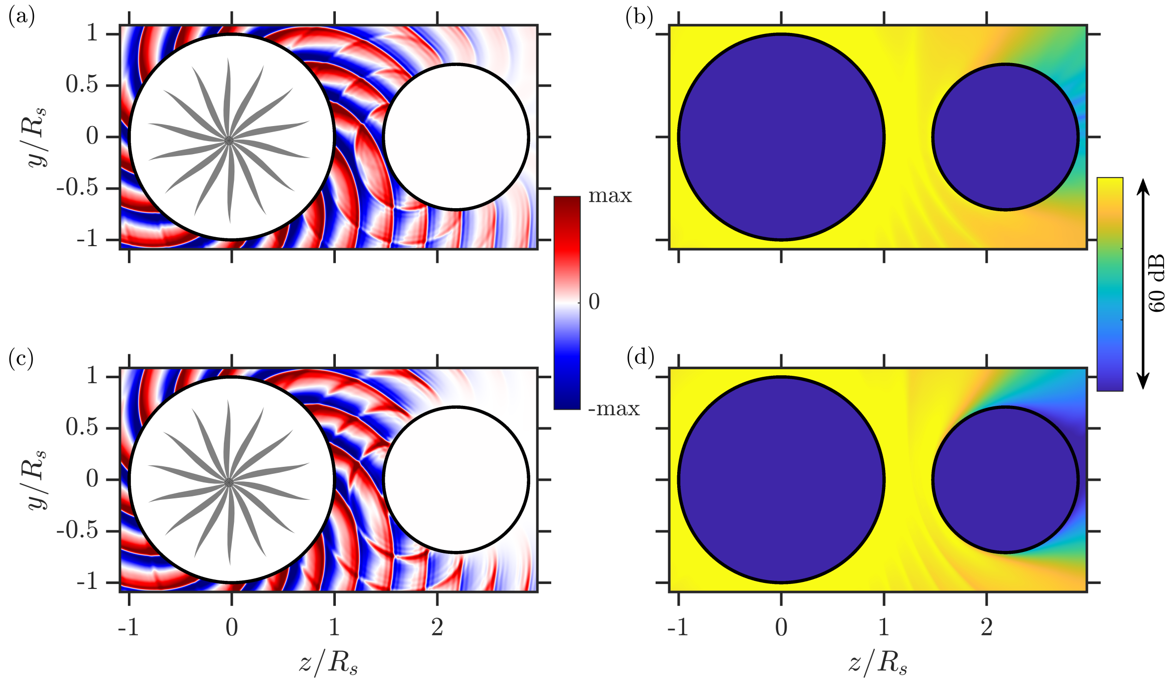

Fig. 8 Snapshots of the acoustic pressure field on the left, and Sound Pressure Level on the right, for a laminar boundary layer, in the yz-plane at $x = 0$ for (a-b) $\delta/R_f = 0$ and (c-d) $\delta/R_f = 0.05$.

Three additional simulations were carried out, each with a boundary layer thickness $\delta/R_f \in [0, 0.1]$. Figure 8 compares the case without a boundary layer to the case with a 0.1 m boundary layer thickness on the yz-plane at $x = 0$. The cylindrical control surface enclosing the unducted single fan engine, represented schematically, is positioned on the left side of the domain, while the fuselage is located on the right. Figures 8(a) and 8(c) show the instantaneous acoustic pressure field at the final iteration. The results indicate that the boundary layer increases the shadow zone for angles θ between 0 and $\pi/2$ and between $3\pi/2$ and 2π. The SPL distributions in Figs. 8(b) and 8(d) further show that the diffraction lobes are reduced in amplitude when the boundary layer is present. However, it is important to note that in a realistic configuration with two engines mounted on opposite sides of the fuselage, no true shadow zone exists. Consequently, the relevant region for this analysis corresponds to θ angles between approximately $\pi/2$ and $3\pi/2$, which represent the area directly exposed to the engine.

The distribution of the acoustic fluctuating pressure over the fuselage surface at the final iteration is presented in Fig. 9 for four boundary layer thickness configurations. As expected, the acoustic pressure reaches its maximum in the vicinity of the rotor plane in all cases, located on the yz plane at $x = 0$. The convective effects induced by the mean flow velocity cause an increase in the wavelength of the pressure signal propagating downstream of the engine, in the positive x direction, while the wavefronts are compressed in the upstream region, towards negative x values. Within the angular range $\theta \in [-\pi/2, \pi/2]$, the diffraction of the acoustic field around the cylindrical fuselage results in a reduction of the acoustic pressure level. Furthermore, a progressive attenuation of the acoustic signature is observed with increasing boundary layer thickness, particularly in the upstream region of the engine. In contrast, the downstream region, in the vicinity of $\theta = \pi$, exhibits a comparatively weaker sensitivity to boundary layer effects. This behaviour is consistent with the results obtained using the ray-tracing method.

The SPL distribution around the fuselage for the four simulations is shown in Fig. 10. As the boundary layer thickness δ increases from Fig. 10(a) to Fig. 10(d), the SPL progressively decreases, particularly in the upstream region at negative x. The diffraction lobes near $\theta = 0$ also vanish upstream for thickness $\delta/R_f \geq 0.025$, as illustrated in Figs. 10(b-d). The shielding effect is strongest for $\delta/R_f = 0.1$, where most of the SPL is concentrated around $\theta = \pi$, corresponding to the region directly exposed to the acoustic waves.

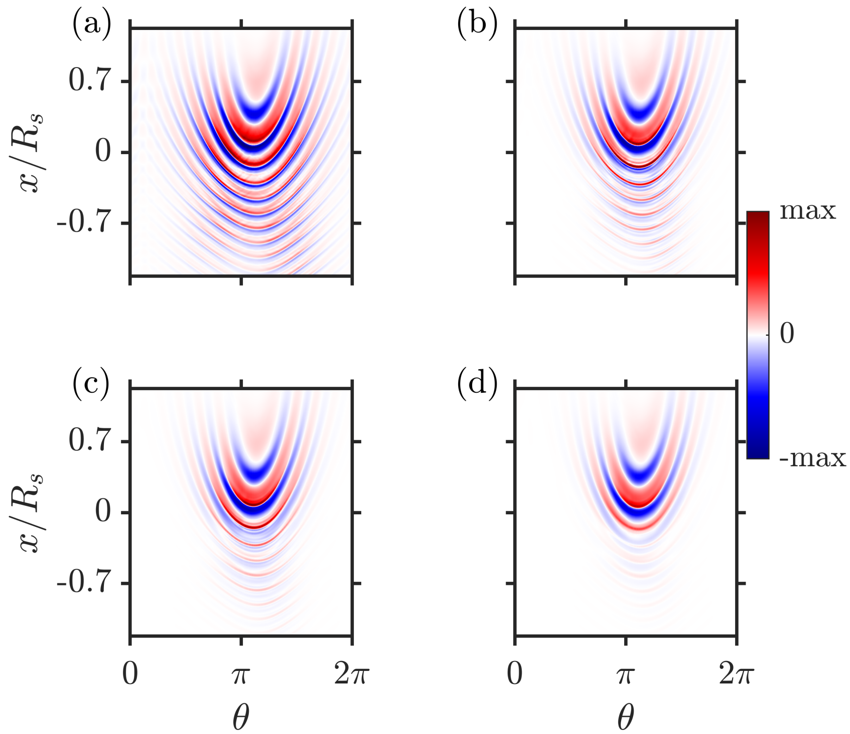

Fig. 9 Snapshots of the acoustic pressure field on the fuselage at the final iteration for a laminar boundary layer with (a) $\delta/R_f = 0$**, (b)** $\delta/R_f = 0.025$**, (c)** $\delta/R_f = 0.05$**, and (d)** $\delta/R_f = 0.1$**.**

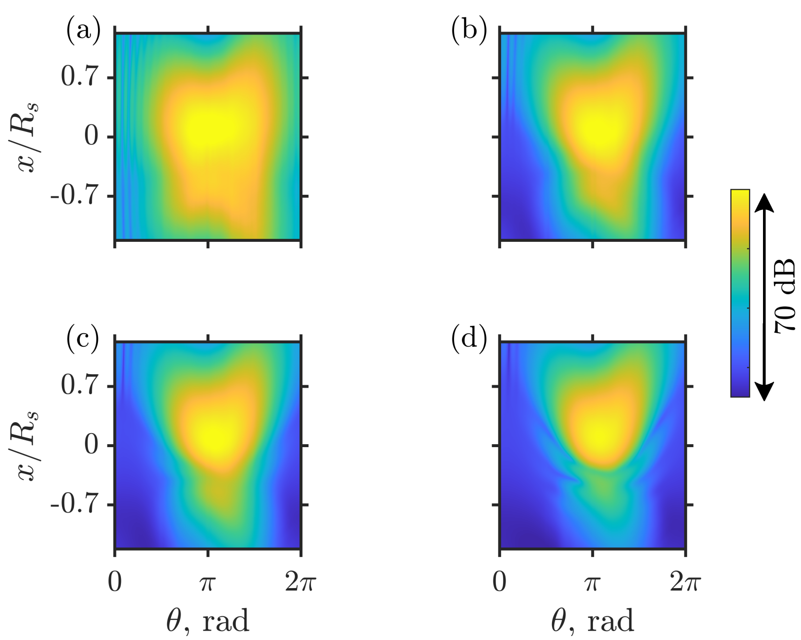

Fig. 10 Sound Pressure Level on the fuselage for a laminar boundary layer with (a) $\delta/R_f = 0$**, (b)** $\delta/R_f = 0.025$**, (c)** $\delta/R_f = 0.05$**, and (d)** $\delta/R_f = 0.1$**.**

The quantity $\Delta\mathrm{SPL}_{BL}$ is introduced as follows:

$$\Delta\mathrm{SPL}_{BL} = \mathrm{SPL}_{\delta} - \mathrm{SPL}_{\delta=0} \tag{4}$$

where SPL_{δ} and $\mathrm{SPL}_{\delta=0}$ are the SPL with and without boundary layer, respectively. A detailed comparison of the SPL for different boundary layer thicknesses δ is presented in Fig. 11. Figure 11(a) shows the SPL distribution along the x-direction at $\theta = \pi$, while Fig. 11(b) reports the corresponding values of $\Delta\mathrm{SPL}_{BL}$ at the same locations. Upstream of the engine, at negative x, a reduction in SPL is observed, which becomes more pronounced with increasing boundary layer thickness. At $x/R_s = -1.17$, the reduction increases from -10 dB for $\delta/R_f = 0.025$ to -25 dB for $\delta/R_f = 0.1$. Downstream of the engine, at positive x, the shielding effect is weaker, with a maximum SPL reduction of approximately -3 dB for $\delta/R_f = 0.1$.

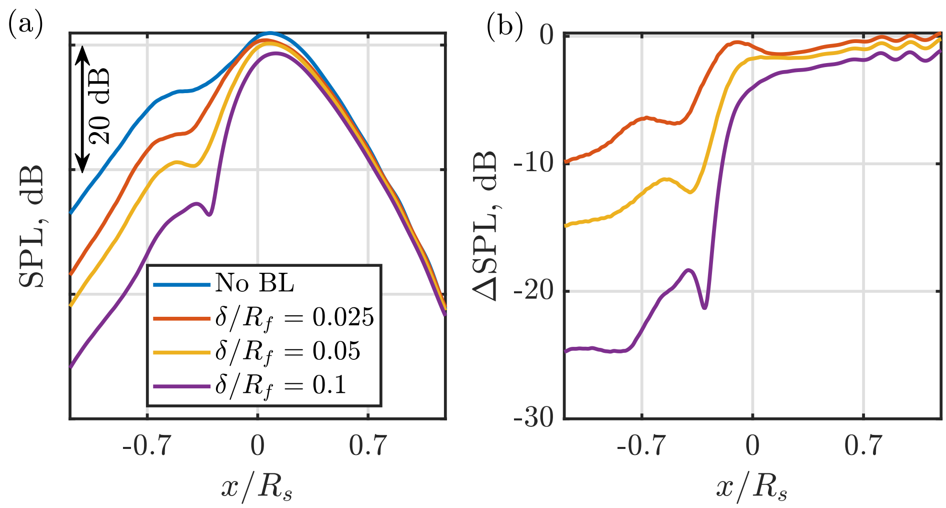

Fig. 11 (a) Sound Pressure Level and (b) $\Delta\mathrm{SPL}_{BL}$ on the fuselage along the x-axis at $\theta = \pi$ for a laminar boundary layer.

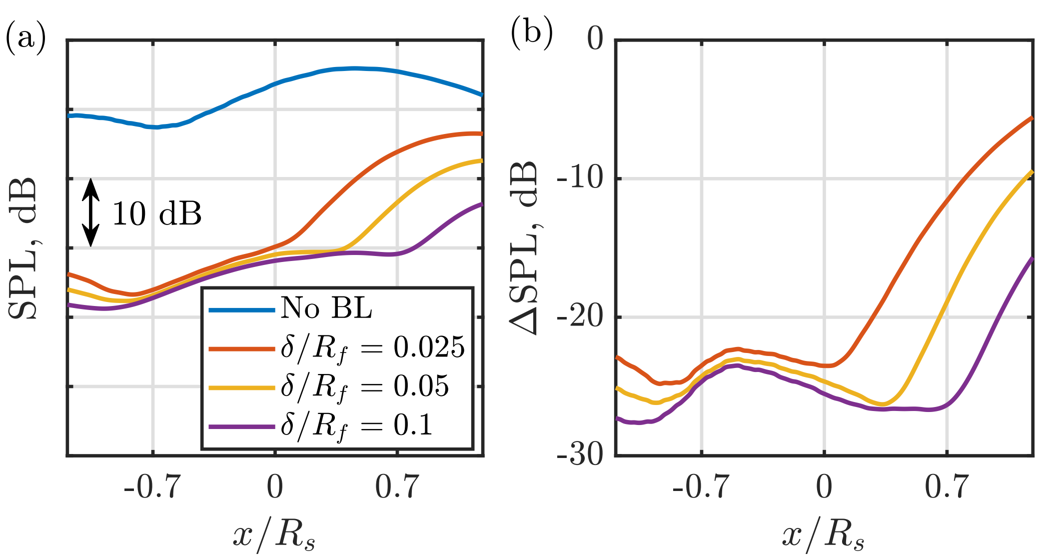

Fig. 12 (a) Sound Pressure Level and (b) $\Delta\mathrm{SPL}_{BL}$ on the fuselage along the x-axis at $\theta = 0$ for a laminar boundary layer.

A similar trend is observed for the SPL along x in the shadow zone at $\theta = 0$, as shown in Fig. 12. The shielding effect is evident upstream of the engine even for $\delta/R_f = 0.025$, with a minimum reduction of -6 dB. This occurs because acoustic waves must travel a longer path around the fuselage in the presence of a velocity gradient to reach the shadow zone, which enhances diffraction effects even for small boundary layer thicknesses δ. In this case, the downstream reduction is also similar to the angular position $\theta = \pi$, reaching up to a minimum of -27.5 dB for $\delta/R_f = 0.1$.

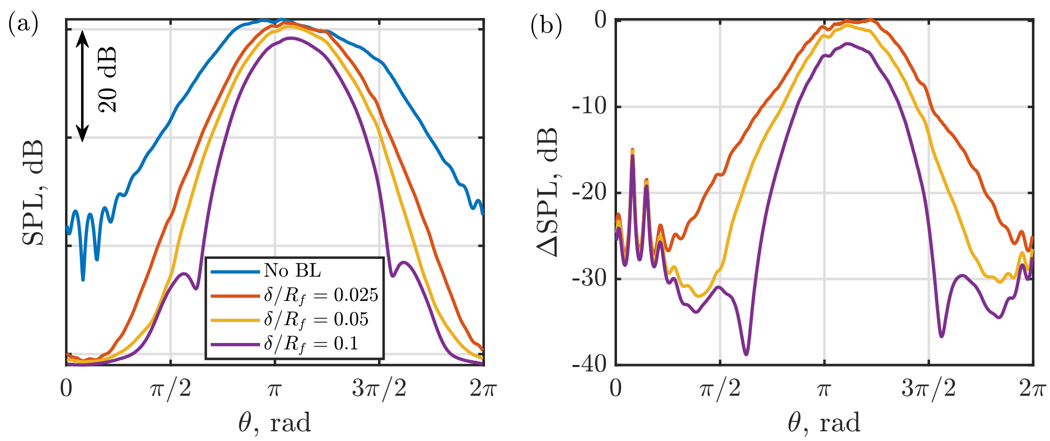

Fig. 13 (a) Sound Pressure Level and (b) ΔSPL_{BL} on the fuselage along the θ-coordinate at $x = 0$ for a laminar boundary layer.

The SPL distribution on the fuselage along θ in the rotor plane at $x = 0$ is plotted in Fig. 13. In Fig. 13(a), the maximum SPL occurs near $\theta = \pi$ and decreases symmetrically on both sides. As the boundary layer thickness δ increases, the peak level decreases and the distribution narrows around $\theta = \pi$. Strong oscillations are observed for $0 < \theta < \pi/4$, corresponding to diffraction lobes, which disappear for $\delta/R_f \geq 0.025$. Figure 13(b) plots the quantity ΔSPL_{BL}, showing that the reduction due to the boundary layer thickness δ is more pronounced in the shadow zone, specifically for $0 < \theta < \pi/2$ and $3\pi/2 < \theta < 2\pi$.

2. Turbulent boundary layer profile

A more realistic boundary layer is prescribed using a semi-empirical model of a turbulent boundary layer, assuming statistically steady conditions and spatial uniformity along the fuselage axis for simplicity. The boundary layer is therefore considered fully developed, with the mean velocity profile depending solely on the wall-normal coordinate expressed in wall units r^+. The model is formulated under the assumption of zero pressure gradient. The mean velocity is expressed in non-dimensional form as

$$U(r^+) = \frac{u(r)}{u_\tau} \tag{5}$$

where u_τ denotes the friction velocity and r^+ is the wall-normal coordinate in viscous units, defined as

$$r^+ = \frac{r u_\tau}{\nu} \tag{6}$$

The boundary-layer thickness δ is defined as the distance from the wall at which the mean velocity reaches the free-stream value u_0. The reference Reynolds number is accordingly defined as

$$Re^+ = \frac{u_\tau \delta}{\nu} \tag{7}$$

with ν denoting the kinematic viscosity of the fluid. The turbulent model, which is integrated in this study, is detailed in [27].

The velocity profiles of the turbulent boundary layer employed in the simulations are presented in Fig. 14. For all three selected boundary layer thicknesses, the model predicts a nearly vertical velocity gradient up to $M = 0.5$ in the region immediately adjacent to the wall. This near-wall viscous region, characterized by a high velocity gradient, is very small relative to the wavelength of the case considered and therefore has a negligible influence on boundary-layer-induced diffraction effects. In contrast, the subsequent region, where the velocity gradient decreases progressively, contributes more significantly to diffraction phenomena. This region extends over a larger spatial range, corresponding approximately to the boundary layer thickness.

The resulting velocity profile is used as the initial condition in the simulations and, in the absence of mechanisms leading to temporal or spatial evolution of the mean flow, remains unchanged throughout the computation.

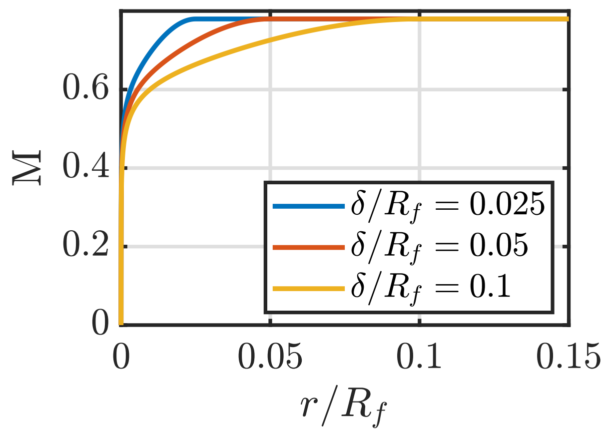

Fig. 14 Turbulent boundary layer velocity profiles for different thicknesses δ.

The distribution of the acoustic pressure field on the fuselage surface in the presence of a turbulent boundary layer is presented in Fig. 15. The results exhibit a behaviour analogous to that observed in the laminar boundary layer case, though with less pronounced effects. A reduction in the acoustic pressure level is observed with increasing boundary layer thickness, with the attenuation being most significant in the upstream region of the engine, towards negative x values.

The SPL distribution on the fuselage surface for different boundary layer thicknesses is presented in Fig. 16, ranging from $\delta/R_f = 0$ in Fig. 16(a) to $\delta/R_f = 0.1$ in Fig. 16(d). Consistent with the previously analyzed laminar boundary layer case, an increase in boundary layer thickness in the turbulent regime leads to a reduction in SPL. This reduction is more pronounced upstream of the rotor and less evident downstream. The maximum SPL occurs at $\theta = \pi$ on the rotor plane at $x = 0$.

A detailed comparison of the SPL distribution along the fuselage x-axis at $\theta = \pi$ is provided in Fig. 17(a). The SPL reaches its maximum near $x = 0$ on the rotor plane, and this peak decreases with increasing boundary layer thickness. Upstream of the rotor, the SPL reduction becomes progressively more significant as the boundary layer thickens, whereas the effect remains comparatively weaker in the downstream region. As shown in Fig. 17(b), the reduction reaches -8 dB for a turbulent boundary layer with a thickness of $\delta/R_f = 0.1$, which is substantially smaller than in the corresponding laminar boundary layer case, where a reduction of -25 dB is observed. This difference is attributed to the turbulent boundary layer velocity profile, which exhibits a very steep gradient in the region immediately adjacent to the fuselage wall, increasing from $M = 0$ at the wall to $M = 0.5$ at the neighboring mesh point in the simulation. The spatial extent of this high–velocity-gradient region is much smaller than the acoustic wavelength of the case considered, which substantially reduces the shielding effect of the turbulent boundary layer relative to that of the laminar boundary layer.

The SPL distribution along the x-axis in the shadow region at $\theta = 0$ is shown in Fig. 18(a) for different boundary layer thicknesses. Overall, a behavior similar to that observed in the region directly exposed to the rotor is identified, with a more significant SPL reduction upstream than downstream. However, the downstream reduction is more pronounced than that observed at the angular position $\theta = \pi$. This difference arises because acoustic waves travel a longer path around the fuselage to reach the shadow region, remaining within the boundary layer for a longer distance and experiencing stronger diffraction effects. The quantity $\Delta\mathrm{SPL}_{BL}$ is plotted in Fig. 18(b), showing a maximum SPL reduction ranging from -18 dB for $\delta/R_f = 0.025$ to -22 dB for $\delta/R_f = 0.1$.

The SPL distribution as a function of the angular position θ on the rotor plane at $x = 0$ is shown in Fig. 19(a). Once again, the maximum peak occurs near $\theta = \pi$, with a symmetric decay on either side of this peak. This decay is accompanied by a progressive narrowing of the curve around the maximum. The oscillations observed near $\theta = 0$ correspond to diffraction lobes in the shadow region of the cylinder; these lobes vanish for $\delta/R_f = 0.1$. The quantity

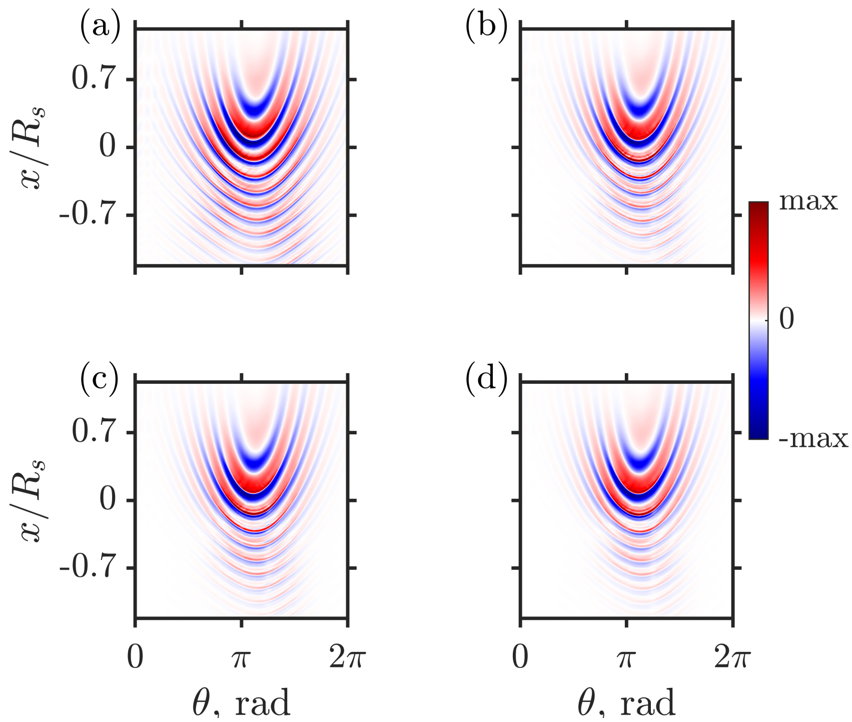

Fig. 15 Snapshots of the acoustic pressure field on the fuselage at the final iteration for a turbulent boundary layer with (a) $\delta/R_f = 0$**, (b)** $\delta/R_f = 0.025$**, (c)** $\delta/R_f = 0.05$**, and (d)** $\delta/R_f = 0.1$**.**

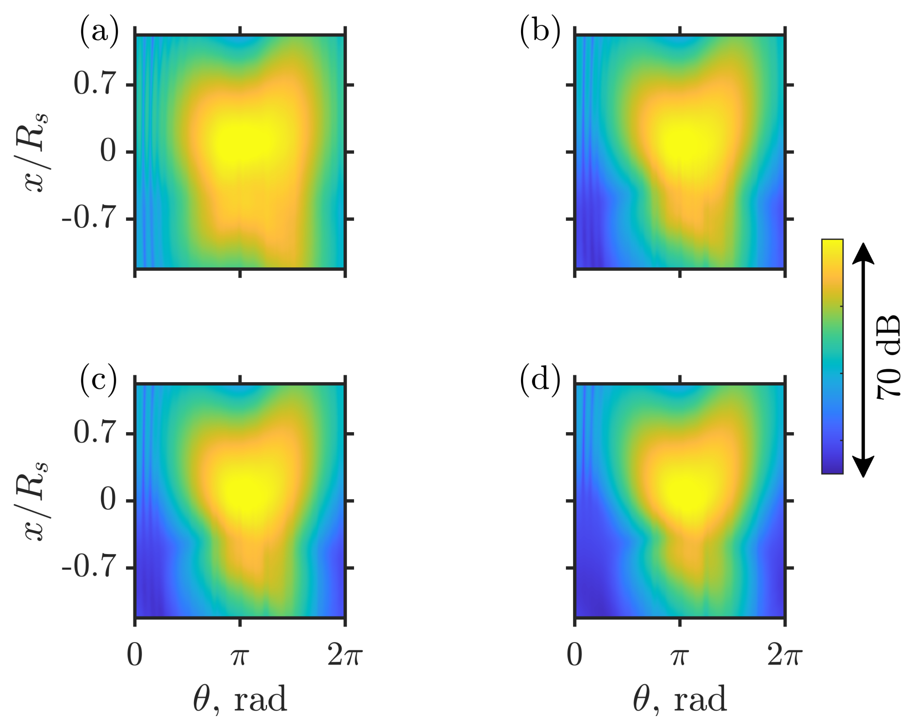

Fig. 16 Sound Pressure Level on the fuselage for a turbulent boundary layer with (a) $\delta/R_f = 0$**, (b)** $\delta/R_f = 0.025$**, (c)** $\delta/R_f = 0.05$**, (d)** $\delta/R_f = 0.1$**.**

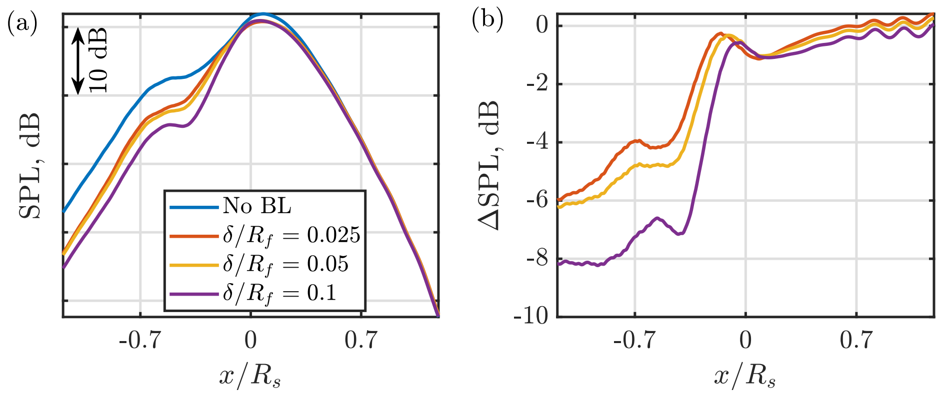

Fig. 17 (a) Sound Pressure Level and (b) ΔSPL$_{BL}$ on the fuselage along the x-axis at $\theta = \pi$ for a turbulent boundary layer.

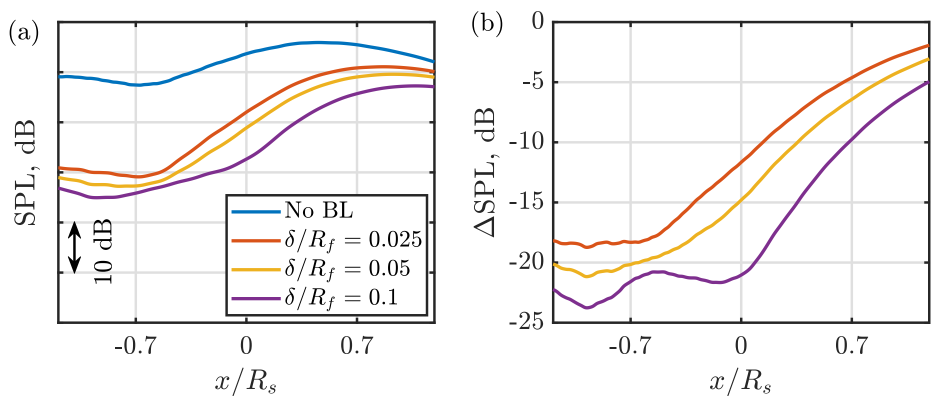

Fig. 18 (a) Sound Pressure Level and (b) ΔSPL$_{BL}$ on the fuselage along the x-axis at $\theta = 0$ for a turbulent boundary layer.

$\Delta\mathrm{SPL}_{BL}$ is plotted in Fig. 19(b). The SPL reduction is less pronounced at $\theta = \pi$, as this location corresponds to the region of direct acoustic wave incidence, where the propagation path is minimal. The reduction becomes increasingly significant with increasing angular distance from the impact point, as the acoustic waves travel a longer path around the cylinder and diffraction effects progressively intensify. The maximum reduction increases from -12 dB for $\delta/R_f = 0.025$ to -25 dB for $\delta/R_f = 0.1$.

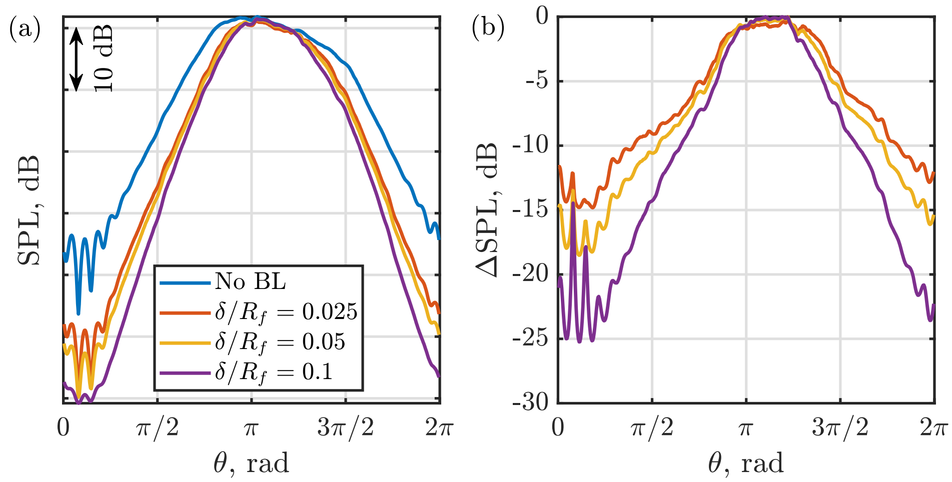

Fig. 19 (a) Sound Pressure Level and (b) $\Delta\mathrm{SPL}_{BL}$ on the fuselage along the θ-coordinate at $x = 0$ for a turbulent boundary layer.

3. Shielding coefficient

The surface sound pressure levels computed on the fuselage for both laminar and turbulent boundary layers of varying thickness indicate that the acoustic shielding effect is more pronounced in the laminar regime. To quantify this noise attenuation, an acoustic shielding coefficient S is introduced, defined as a function of the surface-averaged sound pressure levels obtained with and without a boundary layer. Following the formulation proposed by Gaffney *et al.* [28, 29], the shielding coefficient is expressed as a ratio of surface integrals:

$$S = \frac{\int_A \overline{p^2}_{\mathrm{bl}}\,\mathrm{d}A}{\int_A \overline{p^2}\,\mathrm{d}A} \approx \frac{\sum_N \overline{p^2}_{\mathrm{bl}}}{\sum_N \overline{p^2}} \tag{8}$$

where $\overline{p^2}_{\mathrm{bl}}$ and $\overline{p^2}$ denote the mean square pressure in the presence and in the absence of a boundary layer, respectively, and dA is an infinitesimal surface element on the fuselage. The surface integrals can be approximated by summing the mean square pressure over all N grid elements comprising the fuselage surface. By construction, the coefficient $S \in [0, 1]$, where a value of 0 corresponds to total acoustic shielding and a value of 1 indicates the complete absence of the shielding effect.

The shielding coefficients S for laminar and turbulent boundary layers of varying thickness are shown in Fig. 20(a). The acoustic shielding effect is more pronounced in the laminar case than in the turbulent case, with the difference between the two coefficients increasing with boundary layer thickness. For $\delta/R_f = 0.1$, the coefficient S takes values of 0.25 and 0.55 for the laminar and turbulent cases, respectively.

Figure 20(b) presents the coefficients S^- and S^+, computed from Eq. (8) restricted to the upstream region ($x < 0$) and the downstream region ($x > 0$), respectively, thereby enabling a distinction between the shielding contributions upstream and downstream of the rotor. In both the laminar and turbulent cases, the shielding effect is found to be greater upstream of the rotor than downstream, a result consistent with the trends previously observed in the sound pressure level distributions.

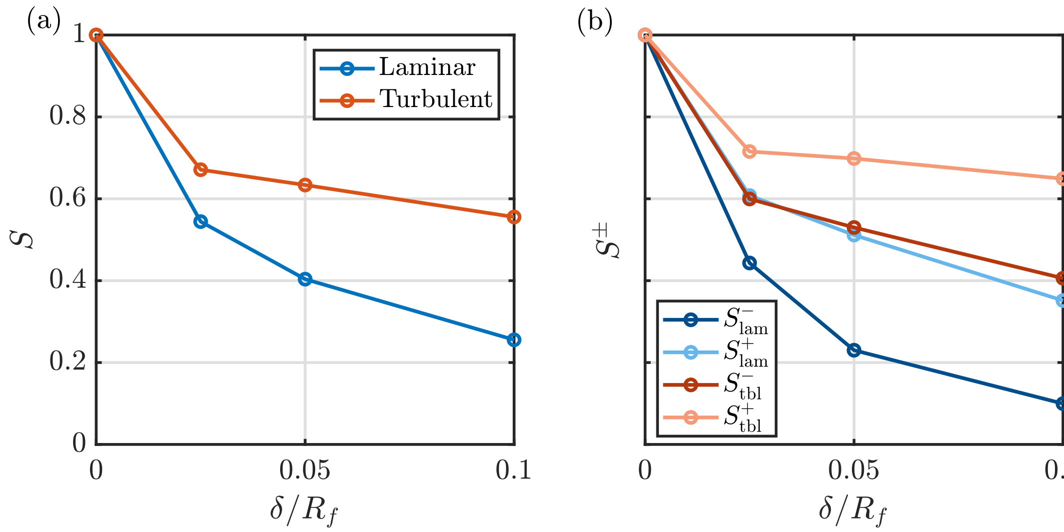

Fig. 20 Shielding coefficient for laminar and turbulent boundary layer (a) over the entire fuselage surface, and (b) exclusively downstream (S^+) or upstream (S^-) of the rotor plane.

IV. Conclusion

A comprehensive numerical investigation of the acoustic loading induced on an aircraft fuselage by an unducted single fan is reported, with particular emphasis on non-linear shock waves propagation and the shielding effect of the fuselage boundary layer. The non-linear Euler equations were solved using source terms derived from a RANS simulation, providing a robust framework for assessing installation effects under cruise conditions.

The results indicate the presence of non-linear effects, particularly for acoustic waves propagating upstream against the mean flow. Their impact on the sound pressure level at the fuselage surface, however, depends on the circumferential position. At $\theta = \pi$, corresponding to the portion of the fuselage directly exposed to the engine, a maximum reduction of approximately 2 dB is observed for upstream-propagating waves. In contrast, at $\theta = 0$, corresponding to the shadow region of the fuselage, the maximum reduction reaches approximately 5 dB. The more pronounced attenuation in the latter case is attributed to the combined effects of cylindrical diffraction and the longer propagation path of acoustic waves around the fuselage. The increased travel distance enhances the cumulative influence of non-linear propagation effects. For waves propagating downstream with the flow, non-linear effects are negligible. These findings address the research objective of evaluating the relevance of non-linear formulations for unducted single fan noise prediction and suggest that linear models can provide a reasonable approximation over large regions of the fuselage, albeit with a slight overestimation of upstream noise levels.

The study identifies sound wave refraction by the fuselage boundary layer as the dominant mechanism governing the acoustic load. A parametric analysis of boundary layer thickness demonstrates a monotonic increase in shielding effectiveness with increasing thickness, with the strongest attenuation observed in upstream and shadow regions. A comparative study between laminar and turbulent boundary layer profiles was performed. For a fixed boundary layer thickness $\delta/R_f = 0.1$, the results indicate that the laminar case provides greater shielding than the turbulent one. In particular, at $\theta = \pi$ upstream of the engine, a maximum reduction of approximately 25 dB is observed for the laminar boundary layer, compared to about 8 dB for the turbulent profile. This disparity is attributed to the smoother near-wall velocity gradients in laminar boundary layers relative to the acoustic wavelength, which enhance refraction effects, whereas the steeper gradients in turbulent boundary layers significantly reduce shielding effectiveness.

Overall, this work advances the understanding of an unducted single fan and airframe acoustic interactions by demonstrating that boundary layer properties exert a substantially greater influence on the fuselage acoustic signature than non-linear propagation effects.

Acknowledgments

This material is based upon work supported by the ANRT (Association nationale de la recherche et de la technologie) with a CIFRE fellowship granted to Giovanni Coco. The study was performed within the framework of the industrial chair ARENA (ANR-18-CHIN-0004-01) co-financed by Safran Aircraft Engines and the French National Research Agency (ANR), and within the framework of the LABEX CeLyA (ANR-10-LABX-0060) of Université de Lyon, within the program "Investissements d'Avenir" (ANR-16-IDEX-0005) operated by the French National Research Agency (ANR). This work was granted access to the HPC resources of PMCS2I (Pôle de Modélisation et de Calcul en Sciences de l'Ingénieur de l'Information) of the École Centrale de Lyon, Écully, France.

References

[1] Lewis, D., Perrin, C., and Falissard, F., "Tonal Noise Predictions of a Generic Open-Fan Based on a Hybrid URANS Approach," *30th AIAA/CEAS Aeroacoustics Conference*, American Institute of Aeronautics and Astronautics, 2024. https://doi.org/10.2514/6.2024-3264.

[2] Hanson, D. B., "Shielding of prop-fan cabin noise by the fuselage boundary layer," *Journal of Sound and Vibration*, Vol. 92, No. 4, 1984, pp. 591–598. https://doi.org/10.1016/0022-460X(84)90201-3.

[3] Hanson, D. B., and Magliozzi, B., "Propagation of propeller tone noise through a fuselage boundary layer," *Journal of Aircraft*, Vol. 22, No. 1, 1985, pp. 63–70. https://doi.org/10.2514/3.45081.

[4] Lu, H. Y., "Fuselage boundary-layer effects on sound propagation and scattering," *AIAA journal*, Vol. 28, No. 7, 1990, pp. 1180–1186. https://doi.org/10.2514/3.25189.

[5] McAninch, G., and Rawls Jr., J. W., "Effects of boundary layer refraction and fuselage scattering on fuselage surface noise from advanced turboprop propellers," *22nd Aerospace Sciences Meeting*, 1984. https://doi.org/10.2514/6.1984-249.

[6] Spence, P. L., "Effects of fuselage boundary layer on noise propagation from advanced propellers," *Journal of Aircraft*, Vol. 29, No. 6, 1992, pp. 1005–1011. https://doi.org/10.2514/3.46277.

[7] Belyaev, I. V., "The effect of an aircraft's boundary layer on propeller noise," *Acoustical Physics*, Vol. 58, No. 4, 2012, pp. 387–395. https://doi.org/10.1134/S1063771012040045.

[8] Brouwer, H., "The scattering of open rotor tones by a cylindrical fuselage and its boundary layer," *22nd AIAA/CEAS Aeroacoustics Conference*, 2016. https://doi.org/10.2514/6.2016-2741.

[9] Gaffney, J., McAlpine, A., and Michael, K., "Sound radiation of fan tones from an installed turbofan aero-engine: fuselage boundary-layer refraction effects," *22nd AIAA/CEAS Aeroacoustics Conference*, 2016. https://doi.org/10.2514/6.2016-2878.

[10] Schippers, H., and Wensing, J. A., "Hybrid computational model for noise propagation through a fuselage boundary layer," *AIAA journal*, Vol. 34, No. 9, 1996, pp. 1785–1792. https://doi.org/10.2514/3.13308.

[11] Rouvas, D. M., and McAlpine, A., "An Analytical Model of Sound Refraction By the Fuselage Boundary Layer for Fan Tone Radiation from a Turbofan Aero-engine," *28th AIAA/CEAS Aeroacoustics Conference*, 2022. https://doi.org/10.2514/6.2022-3059.

[12] Dierke, J., Ewert, R., Delfs, J., Stoehr, C., and Rose, M., "The effect of a boundary layer on engine noise propagating to the fuselage at flight conditions," *19th AIAA/CEAS Aeroacoustics Conference*, 2013. https://doi.org/10.2514/6.2013-2006.

[13] Siefert, M., Delfs, J., and Caruelle, B., "Refraction and scattering in high Mach number boundary layers," *17th AIAA/CEAS Aeroacoustics Conference*, 2011. https://doi.org/10.2514/6.2011-2847.

[14] Howe, M. S., "The role of surface shear stress fluctuations in the generation of boundary layer noise," *Journal of Sound and Vibration*, Vol. 65, No. 2, 1979, pp. 159–164. https://doi.org/10.1016/0022-460X(79)90510-8.

[15] Pridmore-Brown, D. C., "Sound propagation in a fluid flowing through an attenuating duct," *Journal of Fluid Mechanics*, Vol. 4, No. 4, 1958, p. 393–406. https://doi.org/10.1017/S0022112058000537.

[16] Priebe, S., Wood, T., Yi, J., and Mousavi, A., "Large Eddy Simulation of an Open Rotor Fan Blade," *Proceedings of the ASME Turbo Expo 2022: Turbomachinery Technical Conference and Exposition*, 2022. https://doi.org/10.1115/GT2022-80538.

[17] Priebe, S., Jourdan, E., Mousavi, A., Karve, R., Chakrabarti, S., D'Aquila, L., Yi, J., Alhawwary, M., Bharadwaj Ananthan, V., Ramakrishnan, K., and Wood, T., "Large Eddy Simulation of an Open Fan Blade at Full-Scale Reynolds Number," *Journal of Turbomachinery*, Vol. 147, No. 7, 2024. https://doi.org/10.1115/1.4067098.

[18] Daydé-Thomas, V., Polacsek, C., Fauqueux, S., Gloerfelt, X., and Mardjono, J., "Tone noise characterization of an open-fan engine using source-mode integral formulations," *30th AIAA/CEAS Aeroacoustics Conference*, 2024. https://doi.org/10.2514/6.2024-3152.

[19] Lorteau, M., Le Garrec, T., and Daydé-Thomas, V., "Open Fan Noise Confinement Effects in a Closed Wind-Tunnel: Numerical Methodology and Evaluation," *30th AIAA/CEAS Aeroacoustics Conference*, 2024. https://doi.org/10.2514/6.2024-3071.

[20] Lewis, D., Perrin, C., and Falissard, F., "Tonal Noise Predictions of a Generic Open-Fan Based on a Hybrid URANS Approach," *30th AIAA/CEAS Aeroacoustics Conference*, 2024. https://doi.org/10.2514/6.2024-3264.

[21] Polacsek, C., Daydé-Thomas, V., Fauqueux, S., Mardjono, J., and Descamps, M., "Acoustic characteristics of an open-fan model from semi-analytical predictions and wind tunnel tests," *Forum Acusticum Euronoise*, 2025.

[22] Proskurov, S., Dierke, J., Stürmer, A., Ewert, R., and Delfs, J., "Acoustic Simulation for Wing Mounted Open Rotor and Stator," *AIAA SCITECH 2025 Forum*, 2025. https://doi.org/10.2514/6.2025-1817.

[23] Bogey, C., and Bailly, C., "A family of low dispersive and low dissipative explicit schemes for flow and noise computations," *Journal of Computational Physics*, Vol. 194, No. 1, 2004, pp. 194–214. https://doi.org/https://doi.org/10.1016/j.jcp.2003.09.003.

[24] Coco, G., Dragna, D., Bailly, C., and Posson, H., "Injection of acoustic waves via volumetric sources on a control surface for computational aeroacoustics," *The Journal of the Acoustical Society of America*, Vol. 159, No. 2, 2026, pp. 1151–1162. https://doi.org/10.1121/10.0042388.

[25] Hu, F. Q., "Development of PML absorbing boundary conditions for computational aeroacoustics: A progress review," *Computers & Fluids*, Vol. 37, No. 4, 2008, pp. 336–348. https://doi.org/https://doi.org/10.1016/j.compfluid.2007.02.012.

[26] Cambier, L., Heib, S., and Plot, S., "The Onera elsA CFD software: input from research and feedback from industry," *Mechanics & Industry*, Vol. 14, 2013, p. 159–174. https://doi.org/10.1051/meca/2013056.

[27] Prigent, S. L., and Bailly, C., "From shear stress to wall pressure spectra: a semi-analytical approach to account for mean pressure gradients in turbulent boundary layers," *Acta Acustica*, Vol. 6, 2022. https://doi.org/10.1051/aacus/2022034.

[28] Gaffney, J., McAlpine, A., and Kingan, M. J., "Fuselage boundary-layer refraction of fan tones radiated from an installed turbofan aero-enginea)," *The Journal of the Acoustical Society of America*, Vol. 141, No. 3, 2017, pp. 1653–1663. https://doi.org/10.1121/1.4976965.

[29] Gaffney, J., McAlpine, A., and Kingan, M. J., "A theoretical model of fuselage pressure levels due to fan tones radiated from the intake of an installed turbofan aero-engine," *The Journal of the Acoustical Society of America*, Vol. 143, No. 6, 2018, pp. 3394–3405. https://doi.org/10.1121/1.5038263.